Chemistry of shape-controlled iron oxide nanocrystal formation

Chemistry of Shape-Controlled Iron Oxide Nanocrystal Formation

Artur Feld,†,∞,‡, Agnes Weimer†,‡, Andreas Kornowski†, Naomi Winckelmans‖, Jan-Philip Merkl†,∞, Hauke Kloust†, Robert Zierold⊥, Christian Schmidtke†, Theo Schotten∇, Maria Riedner#, Sara Bals‖ and Horst Weller*,†,∞,∇,§*

† Institute of Physical Chemistry, Hamburg University, Grindelallee 117, D-20146 Hamburg, Germany.

∞ The Hamburg Center for Ultrafast Imaging, Hamburg University, Luruper Chaussee 149, D-22761 Hamburg, Germany.

∇ Fraunhofer-CAN, Grindelallee 117, D-20146 Hamburg, Germany.

§ Department of Chemistry, Faculty of Science, King Abdulaziz University, P.O BOX 80203 Jeddah 21589, Saudi Arabia.

Department of Chemistry, Hamburg University, Martin-Luther-King-Platz 6, D-20146 Hamburg, Germany.

‖ Electron Microscopy for Materials Science (EMAT), Department Physics, University of Antwerp, Groenenborgerlaan 171, B-2020 Antwerp, Belgium.

⊥ Center for Hybrid Nanostructures, University Hamburg, Luruper Chaussee 149, 22761 Hamburg, Germany.

KEYWORDS: iron oxide nanocrystals, iron oleate complexes, MALDI-TOF MS, gas chromatography, catalysis, shape control, EELS.

ABSTRACT: Herein we demonstrate that meticulous and in-depth analysis of the reaction mechanisms of nanoparticle formation is rewarded by full control of size, shape and crystal structure of superparamagnetic iron oxide nanocrystals during synthesis. Starting from two iron sources - iron(II)- and iron(III) carbonate -a strict separation of oleate

formation from the generation of reactive pyrolysis products and concomitant nucleation of iron oxide nanoparticles was achieved. This protocol enabled us to analyze each step of nanoparticle formation independently in depth. Progress of the entire reaction was monitored *via* matrix-assisted laser desorption ionization time-of-flight mass spectrometry (MALDI-TOF MS) and gas chromatography (GC) gaining insight into the formation of various iron oleate species prior to nucleation. Interestingly, due to the intrinsic strongly reductive pyrolysis conditions of the oleate intermediates and redox process in early stages of the synthesis, pristine iron oxide nuclei were composed exclusively from wustite, irrespective of the oxidation state of the iron source. Controlling the reaction conditions provided a very broad range of size- and shape defined monodisperse iron oxide nanoparticles. Curiously, after nucleation star shaped nanocrystals were obtained, which underwent metamorphism towards cubic shaped particles. EELS tomography revealed ex post oxidation of the primary wustite nanocrystal providing a full 3D image of Fe^{2+} and Fe^{3+} distribution within. Overall, we developed a highly flexible synthesis, yielding multigram amounts of well-defined iron oxide nanocrystals of different sizes and morphologies.

Superparamagnetic iron oxide nanocrystals (SPION) exhibit exceptional magnetic properties and play a crucial role in various research areas providing the basic concept of many future key technologies.[1] In medicine, SPIONs are used as MRI contrast agents[2,3] and tracers for magnetic particle imaging (MPI).[4] Newly, SPIONs constitute as core components of ceramic-organic nanocomposites with outstanding features opening intriguing perspectives in material sciences.[5] All these applications demand for a superior quality of the nanocrystals (NC). In particular, properties like size, monodispersity, crystal structure and shape are of paramount importance. In order to expand and exploit the scope of technical applications, robust and scalable synthetic routes with full control of these parameters are needed.

Magnetic properties of SPIONs strongly depend, *e.g.* on size, shape and crystal structure. The size not only determines whether the particles display ferromagnetic or superparamagnetic characteristics, but also their saturation magnetization and their blocking temperature[6]. Likewise, the shape of the SPIONs allows manipulation of the magnetic properties.[7] Hence, an irregular shape *e.g.* octapods alters the performance of

T2 weighted MRI[8] and cubic magnetite NC showed a higher blocking temperature, rather than spherical particles.[9] Similarly, three of the most common crystal modifications, namely magnetite (Fe_3O_4), maghemite (γ-Fe_2O_3) and wustite (FeO) differ significantly in their saturation magnetization characteristics.[10] Arrangements of these materials *e.g.* in core-shell composites display exchange bias between a ferromagnetic magnetite shell and a paramagnetic wustite core. This effect is systematically exploited *e.g.* in magnetic sensors and hard drives.[11,12]

However, a purposeful manipulation of the leading triad of size, shape and crystal structure is hampered by numerous intertwined variables, which severely restrict the scope of the synthetic outcome. Hence, the goal of an advantageous synthesis is to unravel these key parameters in order to gain full control over the reaction path. Besides reproducibility and scalability, an optimal synthetic route will offer the flexibility to simultaneously tuning the properties, providing high yields of particles in superior quality.

Herein we introduce iron(II)- and iron(III) carbonate as well accessible iron source for SPION synthesis *via* thermal decomposition of iron oleate. Advantageously, this approach allowed preparation of pure iron oleate, hence not only preventing the influence

of counter ions, like *e.g.* chloride in subsequent steps[8], but even more importantly separating oleate formation and nucleation by a thermal window of at least 80 K. We exploited this feature in a comprehensive study by MALDI-TOF MS in combination with GC for the characterization of various iron specimens along the reaction path.

Here, we show that the chemistry of iron oxide NC formation in the presence of oleic acid is much more complex than hitherto assumed. It includes the formation of polynuclear iron oxide complexes with pronounced redox catalytic properties and ends in pure wustite particles, independent of the valence state and the counter ions of the initial iron source. We will also discuss the role of a polymeric iron oleate network being formed prior to nucleation as well as kinetically and thermodynamically controlled processes during particles growth.

Results/Discussion

Iron sources and their influence on resulting iron oleate (FeOA)

A major obstacle in the high temperature preparation of SPIONs is the purity and composition of the iron oleate (FeOA), on which various syntheses rely on. Therein,

different iron compounds, *e.g.* $FeCl_3$[13], $Fe(acac)_3$[14], $FeO(OH)$[15] and $[Fe(CO)_5]$[16] serve as iron source of FeOA. Subsequent heating generates a series of iron oleate intermediates, which in turn may drive nucleation and growth in very different directions.[17–20] For instance, $FeCl_3$ as iron source may provide different morphologies of SPIONs dependent on the purification process of the iron oleate, *e.g.* remaining chloride ions were believed to induce octapod shape formation.[8,21] Extractive purification of the as-prepared FeOA complex with ethanol and acetone removes chloride ions but results in irreproducible loss of OA molecules.[19] Especially, the ratio of Fe to OA is utmost critical for nucleation and growth of iron oxide NCs. A complete reorganization of the FeOA complexes and a dramatic change of its thermal behavior was reported, indicated by an increase in the iron oxide nucleation temperature, thus decreasing the kinetic separation between nucleation and growth processes and affecting the particle size and particle size distribution.[19] Our experiments with $FeO(OH)$ and $Fe(acac)_3$ indicate the temperature window between the formation of FeOA and the successive steps of intermediates generation (pyrolysis products) often be small and overlapping.

In summary, minute alterations may cause drastic changes in size, size distribution and morphology. Thus, reliable process controls remain a formidable challenge.

Iron(II)- and iron(III) carbonate as iron source

Herein we report a iron source system based on iron carbonates, overcoming utmost all issues, discussed above. Pure iron(II) carbonate was conveniently precipitated by ion metathesis of Na_2CO_3 and $FeSO_4$ under inert conditions. Highly soluble Na_2SO_4 was removed by rinsing with water. In contrast to most iron salts iron(II) carbonate is much more stable than iron(III) carbonate which always contains a large fraction of $Fe(OH)_3$ and FeO(OH). Nevertheless, both iron sources could be exhaustively reacted to FeOA by gentle heating to 60 °C in OA. The decomposition products, namely CO_2 and H_2O were easily removed at 120 °C under vacuum. After removal of water the reaction mixture was of dark brown color, which on further heating gradually brightened up to a clear light yellow solution at 330 °C, suggesting the formation of metal-to-ligand charge transfer complexes.

Iron oleate composition: Profound insight *via* MALDI-TOF MS and GC (TCD)

Herein the high purity of the starting Fe(II) and Fe(III) oleates strongly facilitated elucidation of the complexes formed during the reactions. Numerous FeOA complexes of different composition were identified in the Fe(II) and Fe(III) oleates by MALDI-TOF MS (positive ionization modus) in a mass range of m/z = 350 to 4500. All detectable signals with a S/N >5 were considered and discussed. The mass range of 2 to 20 kDa was analyzed and in contrast to an earlier report, no complexes with higher m/z than 3195 Da could be detected.[18] Unexpectedly, we only found $[M]^+$, but no $[M+H]^+$ molecular ions. This could either be explained by an artifact by iron oxidation in MALDI-TOF during ionization, or by charging due to loss of an oleate molecule (OA^-) [≙ 281.24 Da]. Our data strongly supports the second hypothesis, because the main peak at m/z = 955.6 is hardly to be explained other than loss of oleate as the calculated isotopic distribution shown as well (Fig.1 a). Moreover, MS-MS experiments described below clearly indicate further fragmentation of the observed complexes by loss of oleate (OA^-) ligands.

All reactions for MALDI-TOF analysis were performed with pure (>99.0%(GC)(T)) oleic acid, because linoleic acid, the typical contaminant in the technical grade OA, causes [M-

2]$^+$ peaks, which make adequate analysis more difficult (for more details see section Materials and Methods and SI chapter 4).

Initially, Fe(II)CO_3 resp. Fe(III)CO_3 was reacted with an excess of OA at 60 °C until the end of CO_2 evolution and the formation of a clear solution. The resulting reaction products showed the following signals in MALDI-TOF: m/z = 955.6 - 1,308.7 - 1,590.0 - 1,871.2 - 1,927.2 - 2,208.4 - 2,561.6 - 2,842.8. A compilation of the corresponding mass spectra and by evaluation the mass spectra appropriate iron(II/III) oleate compositions are presented in Fig. 1a. The agreement between theoretical and experimental values is excellent. Heating was continued, and samples were taken under nitrogen and analyzed in approx. 50 K steps (Fig.1b, c).

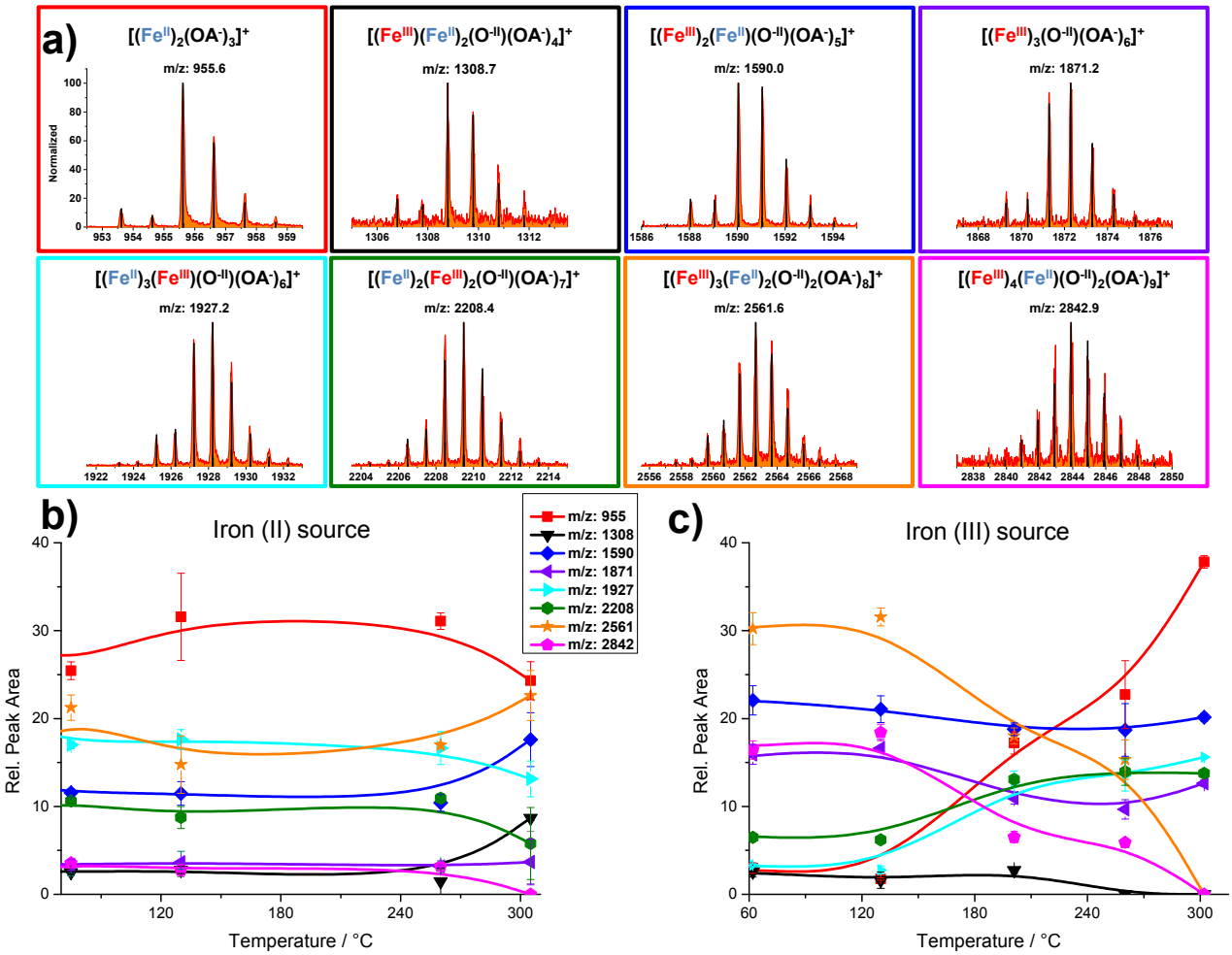

Figure 1. Mass spectra and calculated isotopic distribution with a S/N >5 of formed iron oleates after reaction of Fe(II) carbonate with oleic acid at 60°C and sum formula of the corresponding $[M]^+$ iron(II/III) oleates a). Relative MALDI-TOF MS peak areas measured during the heat-up process of iron oleate resulting from b) iron(II) source and c) iron(III) source at different temperatures.

Surprisingly, the complexes originating from Fe(II) and Fe(III) oleates showed striking similarities even at 60 °C. Eight identical complexes were detected in both series, only differing in intensities (Fig. 1b, c). Similarly astounding is that in early stages of the reaction mostly mixed valence carboxylate bridged iron complexes are formed, indicating redox processes prior to pyrolysis and its associated reduction processes due to H_2 and CO.[17,22] One of a few exceptions to this mixed valences is m/z = 955.6, correlating to a composition of $[(Fe^{II})_2(OA^-)_3]^+$ and being the predominant complex, when starting from iron(II). All complexes are comprised of subunits of oleate(OA^-) as well as iron(II/III) and iron(II/III) oxides. The results were supported by MS/MS spectra of the corresponding molecular ions, *e.g.* the molecular ion of 955.6 Da fragmented into one oleate ion and two Fe(OA) [≙ 337.18 Da] species, thus confirming the former allocation (Figure SI 7). Due to relatively small changes during heating, when starting from iron(II) source, we further describe the temporal evolution of redox processes, starting from iron(III).

Recently it was suggested that the majority of iron(III) oleate contains μ-oxoiron species,[22–26] and consists either of $[(Fe^{III}_3O)(OA^-)_6](OA^-)\cdot 3H_2O$ [22] or $[Fe^{III}_3O(OA^-)_6](OA^-)$

[26]. The structure of the $[(Fe^{III}_3O)(OA^-)_6](OA^-)\cdot 3H_2O$ complex was proposed on the basis of magnetic susceptibility measurements and in both studies experimental data were presented, proving the absence of iron(II). Indeed, we also found the $[(Fe^{III}_3O)(OA^-)_6]^+$ complex (m/z = 1871.2), but beside this pure iron(III) μ-oxoiron complex a number of mixed iron(II)/iron(III) μ-oxoiron complexes have formed as well. However, irrespective of starting with iron(II) or iron(III) source we found even at 60 °C the most frequently represented complexes with masses of m/z = 2561.6, 2208.4 and 1590.0 correlating to a composition as shown in fig. 1a. In case of using iron(II) carbonate as iron source the amount of mixed iron(II)/iron(III) μ-oxoiron complexes with higher content of iron(III) as m/z = 1871.2 and m/z = 2842.9 was significant less represented (Fig. 1b) and reversed if iron(III) carbonate as iron source was used, here m/z = 955.6 and m/z = 1927.2 (Fig. 1c). The occurrence of iron(II)/(III) oleate complexes indicate a redox process in early stages of the reaction.

Remarkably, μ-oxoiron(II)iron(III) complexes are reported to be redox active and therefore used as catalysts for both oxidation and reduction.[27] The catalytic activity for oxidation[28,29] and reduction[30] was shown even at temperatures of 60 °C. Based on these

observations, we propose a mechanism for the reduction, which is due to oxidation of containing complex-bound water and/or oxygen in oxidation state (-II). (As described above, by dissolving iron (II) or iron (III) carbonate in OA water was released).

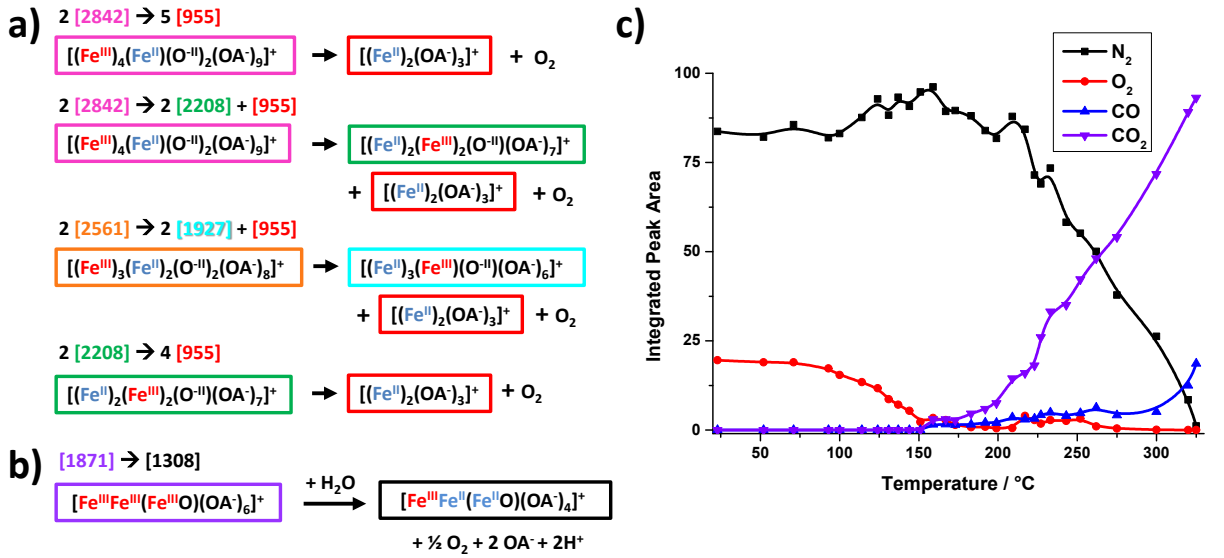

Figure 2. a) Proposed mechanism for the reduction process involving oxidation of oxygen in oxidation state (-II) and the corresponding conversion of the iron oleate complexes b) proposed mechanism for the reduction process involving oxidation of complex-bound water. It should be noted that for all reaction mechanism in a) and b) the formulas of the direct measured m/z were used (loss of one OA^- in each case). As a result of this, in all mechanisms formally molecular oxygen is released, which was proven by gas

chromatography analysis. c) results of chromatography analysis of the control experiment using air instead of nitrogen to demonstrate oxygen consumption (SI chapter 5).

During reaction of iron(III) oleate an increase of the relative peak intensity of m/z = 955.6 ($[(Fe^{II})_2(OA^-)_3]^+$) was observed starting at approx. 150 °C (Fig. 1c). We propose a transition of the mixed valence carboxylate bridged iron complexes to pure iron(II) complex with m/z = 955.6 as shown in Figure 2a. In this mechanism formally molecular oxygen is released, which was proven by head space gas chromatography. Astonishingly, the highest measured oxygen concentration was only 5 % at a reaction temperature of 60 °C, which is below the expected value of quantitative reaction (Figure SI 10). With increasing reaction temperatures no further oxygen could be detected. We supposed that the released oxygen was consumed by redox reactions within the solution. As shown in a control experiment (particle synthesis under aerobic conditions) (Fig. 2c) the entire oxygen is consumed by chemical reactions starting already at temperatures below 100 °C. Oxygen consumption at such low temperatures may be due to the catalytic activity of (μ_3-oxo)triiron cluster at m/z = 1590.0. Ito *et al.* reported the catalyzed

epoxidation of olefinic alcohol acetates by molecular oxygen in presence of (μ_3-oxo)triiron cluster complexes already at 60 °C.[28] Another control experiment using OA and air under the same conditions, however the absence of iron, showed increased consumption of oxygen only after heating to above 140 °C, supporting the catalytic role of iron/ iron oleate complexes in this process (Figure SI 11).

Degradation of OA starts at approx. 150 °C as indicated by the formation of CO_2 and CO. Note that this temperature window lies in the range of FeOA production, when other frequently used iron sources like iron hydroxide or acetylacetonate are used. In these cases FeOA formation and degradation happens concomitantly and is, thus, a serious obstacle in controlling the reaction conditions. By using iron carbonate as iron source FeOA formation is strictly separated from iron oxide intermediates formation by a large "thermal window" of about 80 K. No significant changes of the FeOA complexes can be observed in the temperature range of 60 °C to 140 °C (Fig. 1 b-c). While taking samples in the temperature range between 320 – 340 °C we observed an increase in viscosity and a slight increase of the boiling point. During this reaction period all FeOA complexes formed at lower temperatures decreased in intensity and disappeared shortly after

nucleation as indicated by MALDI-TOF. Instead, we observed peaks, which cannot be assigned to well-defined FeOA complexes. The measured masses most probably stem from iron complexes formed by degradation products from pyrolysis of OA as indicated by the isotopic distribution in MS. The observed viscosity increase might be explained by the formation of a network in which iron(II) is acting as network nodes and crosslinked OA as interconnecting bridges. This explanation is supported by the recent finding that crosslinking of OA *via* their double bonds occurs in pressed powders of iron oxide NC in exactly this temperature range.[5] Bi- or multi-functional alkyl species with terminating COO^- groups were formed during this process serving as interconnects between iron oxide NC and leading to nanocomposites with outstanding mechanical properties. Once started, the reaction quickly became vigorous under bubble formation, accompanied by a decrease in viscosity and rapid particle formation. The decrease in viscosity can be explained by a degradation of the proposed iron oleate network, which is initiated by COO^- decomposition under formation of CO and FeO monomers. In this sense, the breakdown of the network and the associated release of FeO monomers might be understood as a key element for separating nucleation and growth.

Enhanced size and shape controlled synthesis

We demonstrate that irrespective of the oxidation state of the iron carbonate -(II) or (III)- in each case SPIONs of identical shape, size and crystal structure were obtained, indicating a similar reaction mechanism during nanoparticle formation. The uniformity of the resulting FeOA enables an enhanced size and shape controlled synthesis. For example, SPIONs of different shape with narrow size distribution and high uniformity could be prepared only by changing the concentration (Fig 3a,b). For XRD measurements samples were taken under strictly inert conditions and measured in sealed capillaries to prevent a partial post-synthetic surface oxidation which occurs usually during routinely purification under aerobic conditions, as also recently reported by Chen *et al.* and Kemp *et al.*[22,31] Both iron sources furnished SPIONs exclusively displaying a wustite (FeO) structure, as comprehensively proven *via* XRD (Fig. 3c).

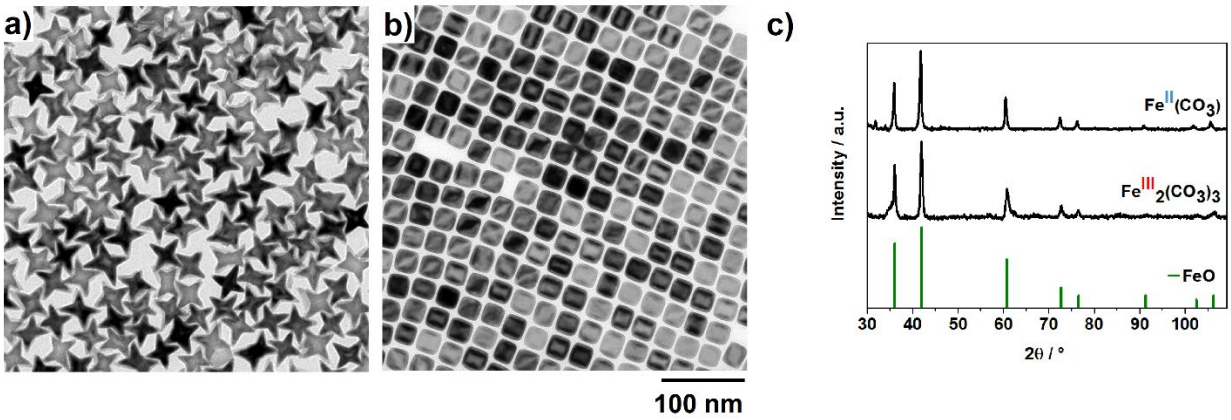

Figure 3. a, b) TEM images of SPIONs synthesized with different initial concentrations of FeOA (66 vol% oleic acid and 34 vol% 1-octadecene (a) and 92 vol% oleic acid and 8 vol% 1-octadecene (b) (both identical Fe:OA ratio of 1:7). c) XRD pattern of iron oxide samples synthesized with iron(II) carbonate and iron(III) carbonate as initial iron source. All measurements were carried out in a sealed capillary under inert condition. As reference wustite 00-006-0615 (FeO) is shown in c).

As a result of investigation how shape and size is affected by reaction parameters such as reaction time, ratio of Fe/OA and concentration (see Figures SI 14 – SI 17 for more details) we found that the “star-like” shape SPIONs only can be obtained shortly after nucleation in early stages of the reaction. In the further course of the reaction they transformed into cube shape structures. Figure 4 illustrates a short overview of possible

sizes and shapes that can be synthesized using this approach (a detailed overview can be found in the supporting information in chapter 8). The nanocrystals can be prepared in quantities up to 20 grams per batch as indicated in the experimental section.

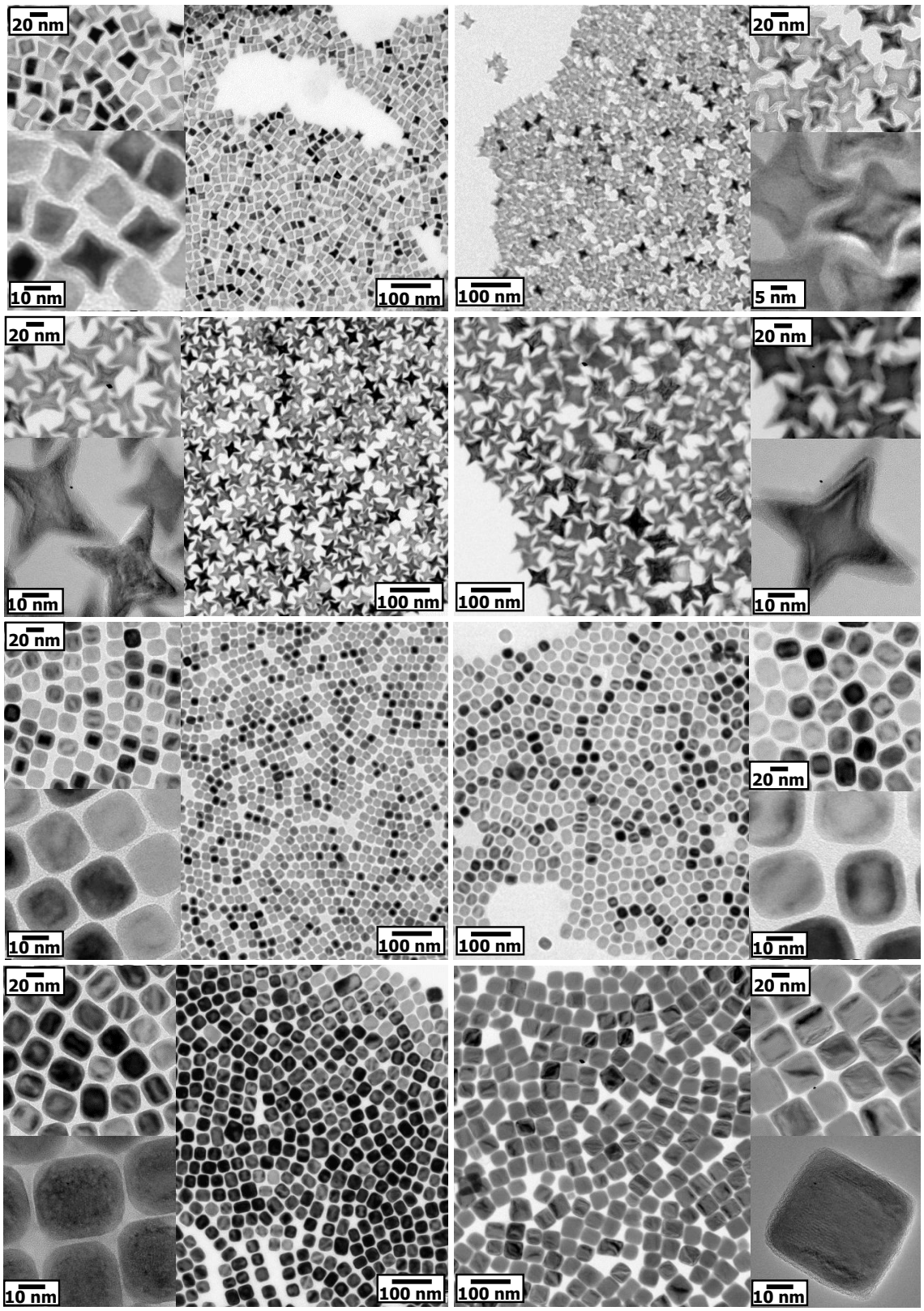

Figure 4. Short overview of TEM images of star-shaped and cubic nanocrystals which

can be synthesized by this approach.

To get a deeper insight of the real 3D structure of the “star-like” shape SPIONs (Fig 3a and Fig 4) the particles were elucidated *via* electron tomography and SEM. Comparison of TEM, STEM, SEM images and a 3D visualization of a particle obtained by electron tomography (Fig. 5) immediately reveals the octapod shape, containing eight triangular pods. When performing electron tomography, a tilt series of 2D HAADF-STEM images was recorded, covering a tilt range of ±76°. The reconstructed 3D model is in excellent agreement with the octapod shape (Fig. 5).

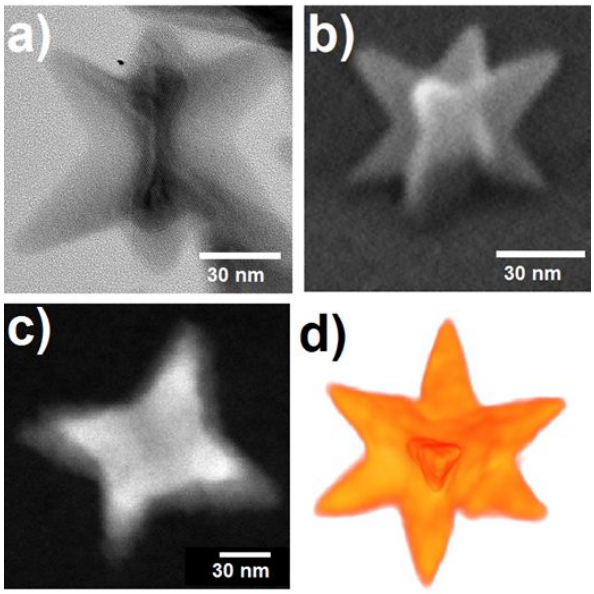

Figure 5. Structure elucidation of an iron oxide octapod sample by electron microscopy imaging and electron tomography. a) TEM image, b) SEM image (70° tilted) (a more detailed presentation is illustrated in figure SI 13) and c) STEM image of a single octapod. d) 3D reconstruction of a nanocrystal based on electron tomography, which can be considered as octapod containing eight triangular pods.

The surface facets of the NCs were further investigated using high resolution HAADF-STEM. It should be noted that the samples, which were used for these measurements and the EELS tomography (see below) were partially oxidized due to storage under ambient conditions, and that the degree of oxidation might vary between the samples shown in Fig. 6 and 7. Remarkably, we did not detect differences in shape and size of the SPIONs compared to non-oxidized samples. The oxidation led to a partially transformation from wustite to magnetite and/or maghemite, as shown below. All these crystalline phases exhibit an fcc sublattice of oxygen, meaning that the assignment of growth direction and faceting does not depend on the degree of oxidation. A high resolution image of a single pod of a NC acquired along the [110] direction is presented

in Figure 6a. Its Fourier analysis (Figure 6b), clearly indicate a growth direction of the pod along the [111] direction, in agreement with previous studies.[8] To investigate the side facets of the pod, a thickness profile (Figure 6e) is extracted from the high resolution HAADF-STEM projection as indicated by the white rectangle in Figure 6a. From that it is evident that the left facet is imaged edge on whereas the other two facets are inclined with respect to the projection direction (Figure 6d). From the FFT pattern, we conclude that the side facet corresponds to a {113} facet composed of alternating (100)/(111) terraces and steps, lowering the surface energy of the NCs, again in agreement with previous investigations.[8] A model of the facets is provided in Figures 6c-d.

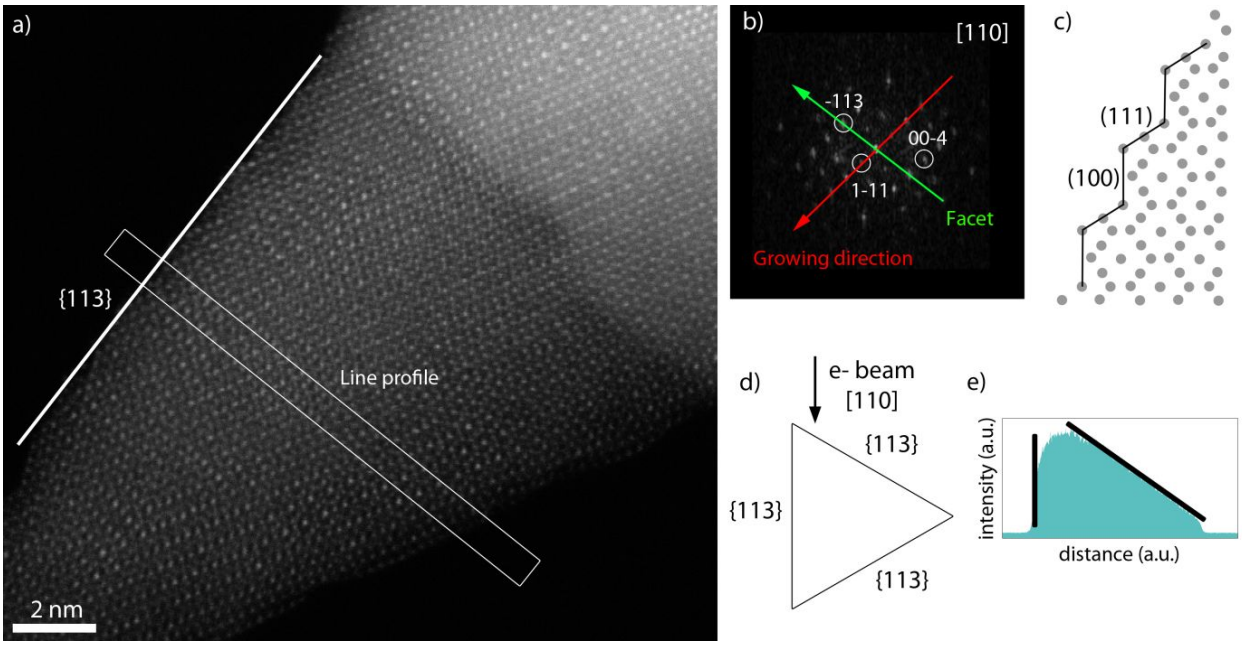

Figure 6. a) High resolution HAADF-STEM projection of one pod of an iron oxide NC oriented along the [110] direction. b) FFT of image from which the growing direction and the side facet can be determined. c-d) Models of the {113} facets of the triangular pod. The facets are composed of alternating (100)/(111) terraces and steps. e) The intensity profile acquired along the direction indicated in a). The profile is in agreement with a triangular morphology composed of {113} facets as indicated in d).

To determine which iron oxide phases are present after partial oxidation, a Fourier analysis of a high resolution STEM image (SI, chapter 6) was performed and a biphasic core /shell structure was observed. A characteristic that can be used to differentiate between the different phases is the valency of iron: for maghemite Fe^{3+} is expected, whereas in magnetite both Fe^{2+} and Fe^{3+} occur. In wustite only Fe^{2+} is present. The fine structure of monochromated electron energy loss spectroscopy (EELS) enables one to determine the valency of iron within the NC (Fig 7).[32] Figure 7c shows EELS spectra acquired in the middle and near the edge of the particle respectively. Both spectra contain features suggesting the presence of Fe^{2+} and Fe^{3+}, but the peak corresponding to Fe^{3+} is

more significant near the edge of the particle. Both spectra can be considered as 2D averages of the overlapping of different proportions of Fe^{2+} and Fe^{3+} located in various volume fractions of the real 3D structure (*e.g.* core and shell). As mentioned above, the as prepared pure wustite NCs were partially oxidized and thus different phases of iron oxide (*e.g.* wustite, maghemite, and magnetite) could have occurred. To distinguish between the different iron oxide phases it is essential to determine the spatial distribution of Fe^{3+} and Fe^{2+}, thus, to combine EELS with tomography. Such studies are very challenging, but recently, first results have been published.[32–38] By using the so-called direct spectroscopic tomography technique[32], fifteen EELS data cubes were combined into a reconstruction of voxels containing Fe^{2+} and a reconstruction with the voxels that contain Fe^{3+}. The result, illustrated in Figure 7, confirms a core/shell like morphology. Slices through the reconstructions demonstrate that the core of the NC only contains Fe^{2+}, in agreement with the wustite structure, whereas at the edges Fe^{3+} is clearly dominant, indicating maghemite structure. It is also seen that there is no sharp interface between Fe^{2+} and Fe^{3+}, but that the Fe^{2+} signal gradually decreases towards the surface. This

finding suggests that the oxidation of wustite to maghemite occurs *via* intermediate formation of magnetite or mixed phases, in accordance with literature data.[22,39–41]

Magnetic measurements corroborate the aforementioned results of core/shell nanoparticles (Fig SI19-21). A temperature-dependent exchange bias pinpoints to a coupling between an antiferromagnetic and a ferromagnetic layer.[42] In detail, the observed exchange bias in the hysteresis curve vanishes at temperatures above 200 K indicating that the Néel temperature of the antiferromagnet has been overcome. Note, T_N has been reported to be around 200 K for wustite.[43] This transition can also be observed in temperature-dependent measurements of the magnetic moment. In addition to the transition at 200 K, a second transition at around 125 K can be revealed. We attribute this feature to the Verwey transition at which magnetite undergoes a metal-insulator transition with a slight lattice rearrangement and a modification of all electronic related properties.[44] Based on these magnetic measurement results, one can conclude the existence of a core/shell nanoparticle consisting of wustite and magnetite.[39] Moreover, depending on the size of the particles, which evolves with time during preparation (compare phase 1 to phase 4 in Fig. 8), the single-domain superparamagnetic behavior indicated by a closed

hysteresis at 300 K and a magnetic field-dependent maximum in the zero-field-cooled measurement evolves into a ferromagnetic state (open hysteresis at 300 K).

In summary, our results also explain the difficulties in selective post-preparative oxidation of wustite into magnetite NC, and make clear that, especially for larger SPIONs, well-defined oxidation conditions need to be elaborated.

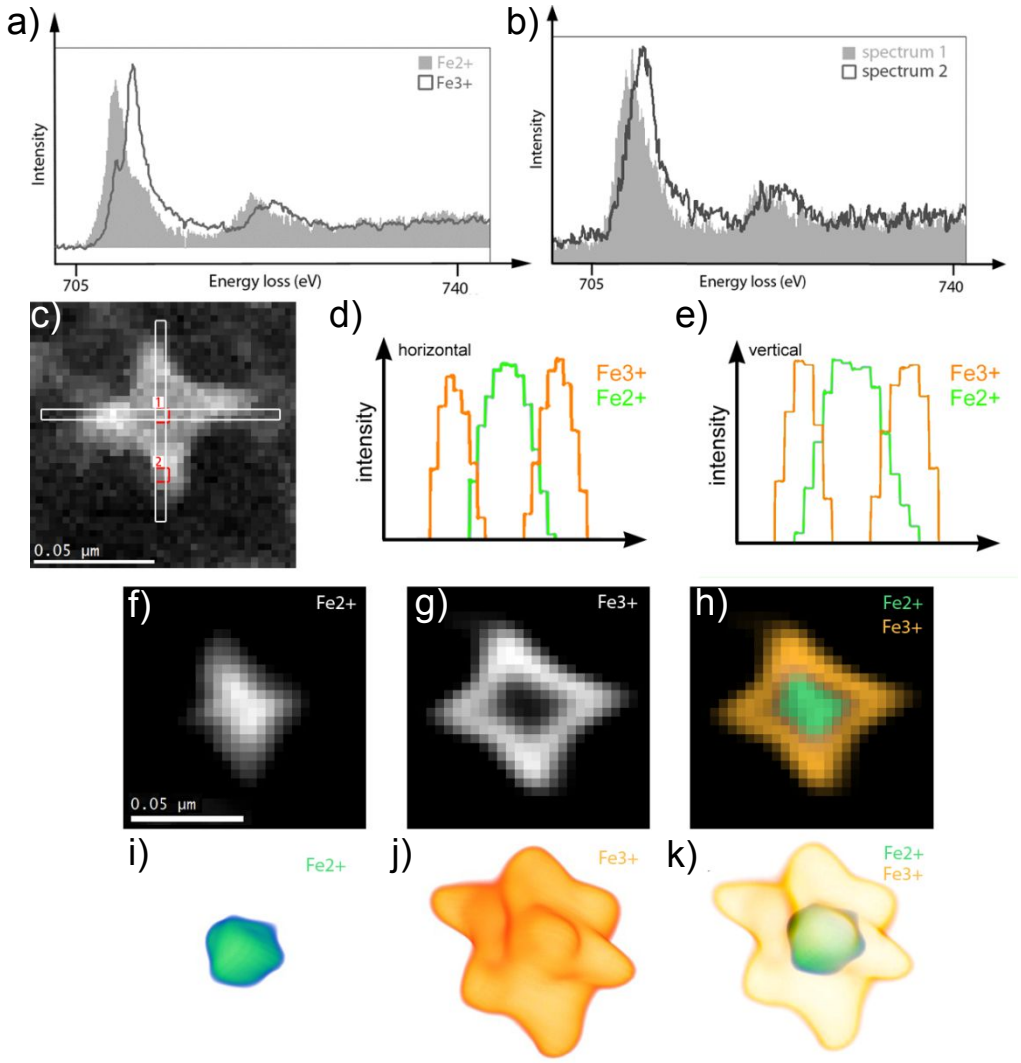

Figure 7. TEM direct spectroscopic tomography of an oxidized octapod sample. a) Reference spectra of Fe^{2+} and Fe^{3+} $^{+}$ acquired from an ilmenite ($FeTiO_3$) and hematite (Fe_2O_3) sample.[32] b) EELS spectra of regions indicated (red squares) in image c). c) 2D HAADF-STEM image of the region on which EELS was performed and line profiles in horizontal and vertical direction were performed d,e). f-h) Slice through the reconstruction

of Fe^{2+}, Fe^{3+} and the overlap of both slices respectively. i-k) 3D reconstruction of Fe^{2+}, Fe^{3+} and the overlap of both reconstructions respectively.

Crystal growth and metamorphosis depend on the thermodynamic and kinetic control of the reaction conditions. Khurshid *et al.*[45] pointed out that *e.g.* octapod star-shaped SPIONs are the kinetically favored product. These findings were supported by Bau *et al.*[46], demonstrating that the shape of mixed metal oxide nanoparticles comprised of iron and nickel can be manipulated *via* ligand concentration and reaction time. However, the nickel content poses severe issues on applications in cell experiments or in living organisms.

Interestingly, we observe that metamorphism of SPIONs is similar to the processes, well described for metallic NPs (Au, Pt, and Pd), as well as MnO_2.[47,48] Gold, platinum, palladium und manganese oxide form a cubic face centered crystal lattice and the formation of special shapes like octapods is explained as a result of high coverage of the {100} side facets of a cuboctahedral core under the influence of atom deposition and surface diffusion.

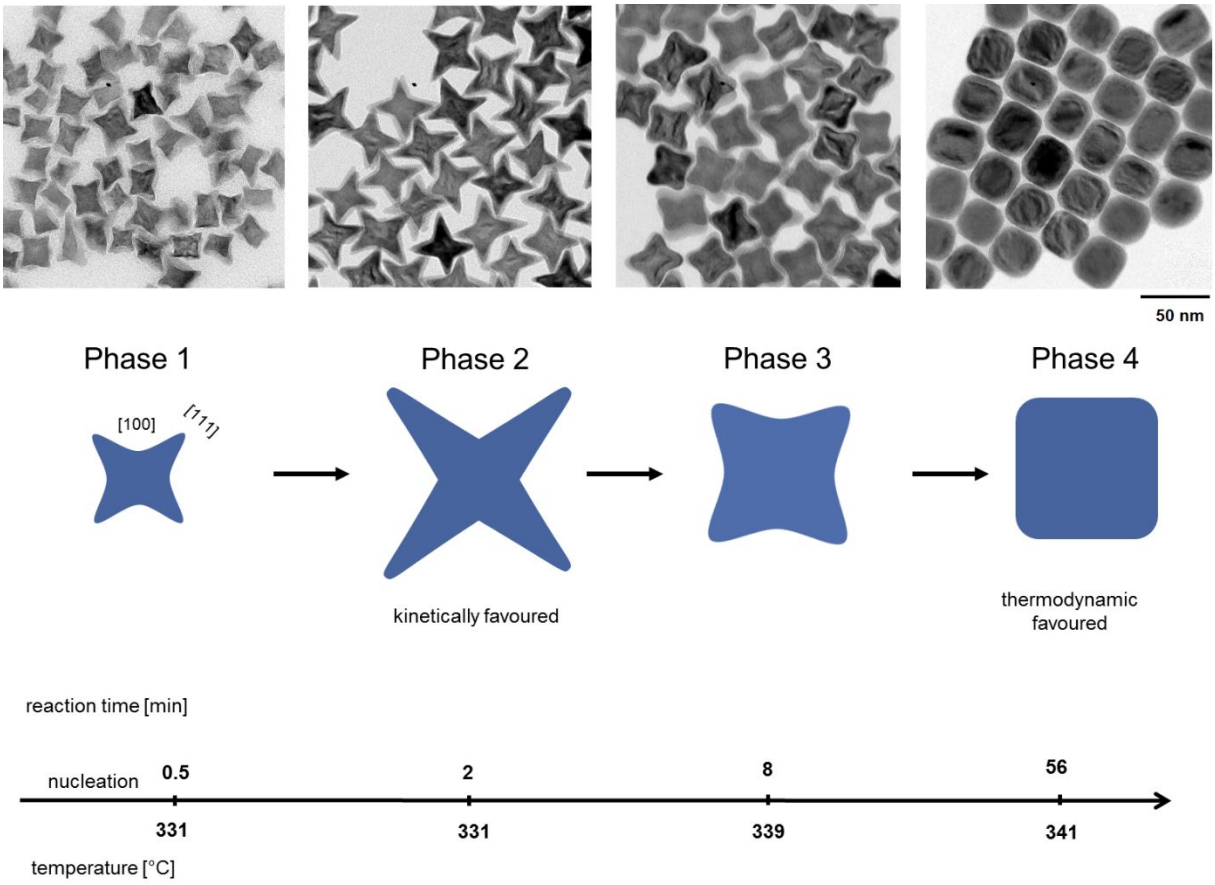

Figure 8. TEM images of particle size and shape formation during one hour of reaction and a corresponding scheme of the different development stages (Fe/OA = 1:7; 1-octadecene = 8 vol%).

The octapod is kinetically favored, and generated as far as the deposition rate of the FeO monomer is significantly higher than the diffusion rate at the surface of the NC. In

our case, we can distinguish four reaction regimes: Similar to the argumentation for nucleation and growth of cubic PbSe[49] we propose that in the initial reaction phase nucleation and growth leads to tiny cubes with {100} and {111} facets (phase 1). OA strongly stabilizes the {100} facets leading to preferential growth in <111> directions under kinetic control in phase 2. A spotlight on beginning of this process is seen in Fig. 8 (Phase 1) where some particles still more resemble cubic shape and others already have started metamorphosis to octapods. Formation of the latter is completed after 2 min. (Fig. 8/Phase 2) under kinetically controlled focusing conditions, *i.e.* the excess FeO monomers grow on already existing particles (reaction phase 2). After that time all monomer is consumed. During the third reaction phase (approximately 8 minutes) the octapods gradually smoothen, resulting in cubes with slightly truncated corners (Fig. 8/Phase 3). Note that the edge length of the NC decreases in this time window, indicating that shape transformation is mainly dominated by surface diffusion of atoms migrating to the edges and side facets, driven by thermodynamics.[47] For longer reaction times (phase 4) Ostwald ripening becomes the dominant mechanism, *i.e.* large cubes grow on the cost

of smaller ones, also driven by thermodynamics (Fig 8/Phase 4) (a more detailed presentation is illustrated in figure SI 18).

We further investigated how dilution with non-coordinating 1-octadecene (ODE) influences size and shape formation under high OA to Fe ratio (7:1) conditions (Fig SI 14). In summary, it can be seen that the largest octapods were obtained in pure OA, whereas already moderate dilution (8 vol%) revealed to a strong decrease in size. Because the octapod formation occurs in the focusing regime of crystal growth (phase 2, see above), we conclude that dilution strongly accelerates the nucleation rate (see SI chapter 8 for more details). We also observe a significant lower increase in viscosity upon dilution prior to nucleation. It is, therefore, reasonable that the proposed iron oleate network is most pronounced in pure OA and retards FeO monomer release. Dilution also leads to lowering the driving force for blocking the {100} facets with OA. At highest dilution (66 vol%) nucleation is obviously so fast and blocking of {100} facets so ineffective that octapod formation is completely suppressed and cube shaped particles formed instead. The same was observed when the OA to iron ratio was reduced and the cubes became smaller upon dilution (see Figure SI 17).

Conclusions

In conclusion, we could not only develop synthetic protocols allowing gram scale production of highly monodisperse SPIONs of various well-defined sizes and morphologies. It furthermore allowed us to identify a complex redox cascade during formation and transformation of polynuclear iron oleate complexes and the formation of a polymeric iron oleate network prior to nucleation. The results enabled us to clearly work out kinetic and thermodynamic effects during nucleation and growth. To the best of our knowledge, we here presented one of the best understood investigation on the chemistry of nanocrystal formation.

Methods/Experimental

Materials. All chemicals were used as received unless otherwise stated. Chemicals (Purity [%], Purchased from): acetone (99.0, Th. Geyer); acetone (dry max. 0.01% water)(99.0, AppliChem); chloroform (dry)(≥99, Sigma-Aldrich); helium 5.0 carrier gas (99.999, Westfalen); hydrochloric acid (37, VWR Chemicals); iron(II) sulfate

heptahydrate (degassed and stored under nitrogen) (99.0, Sigma-Aldrich); iron(III) sulfate (degassed and stored under nitrogen) (97, Sigma-Aldrich); oleic acid (technical grade) (degassed and stored under nitrogen) (90, Sigma-Aldrich); oleic acid (pure) (99.0, TCI Chemicals); 1-octadecene (90, Sigma-Aldrich); sodium carbonate (degassed and stored under nitrogen) (dry basis) (99.95-100.05, Sigma-Aldrich); sulfuric acid (95, Th. Geyer); tetrahydrofuran (99.7, VWR Chemicals); toluene (dry) (99.85, Acros Organics); toluene (100, VWR Chemicals); 9-nitroanthracene (HPLC grade) (degassed and stored under nitrogen) (≥98.5, Sigma-Aldrich); molecular sieve adsorbent 5A 45/60 mesh (Supelco).

Synthesis of the iron sources. All reactions were carried out under Schlenk conditions, using nitrogen as protective gas. Due to the high sensitivity towards oxygen, the reaction apparatus was degassed four times using evacuate-refill cycles. Milli-Q water (18,2 MΩ/cm) was used and saturated for 24 hours with nitrogen. The oleic acid and the 1-octadecene were degassed (25 °C, 1 h, $5*10^{-1}$ mbar) before use and also saturated with nitrogen.

Synthesis of $FeCO_3$ - iron(II) source. $FeSO_4 \cdot 7\ H_2O$ (14.30 g, 51.44 mmol) and Na_2CO_3 (16.40 g, 157.7 mmol) were separately dissolved in degassed water (each 180 mL). The $FeSO_4$-solution was slowly added to the Na_2CO_3-solution and was stirred at 800 rpm over a time period of 30 min at room temperature. The $FeCO_3$ precipitates and was filtered in a Schlenk-frit (reaction equation (1) is shown in SI chapter 1.1). After filtration it was washed with water (4x120 mL), separating highly soluble Na_2SO_4. The resulting grey precipitate is shown in figure SI 1.

Synthesis of $Fe_2(CO_3)_3$ – iron(III) source. $Fe_2(SO_4)_3 \cdot x\ H_2O$ (15.90 g, 39.76 mmol) and Na_2CO_3 (13.60 g, 128.3 mmol) were separately dissolved in water (180 mL). The $Fe_2(SO_4)_3$-solution was slowly added to the Na_2CO_3-solution and was stirred at 800 rpm over a time period of 30 min at room temperature. The resulting reddish-brown precipitate was washed with water (4x120 mL) (reaction equation (2) is shown in SI chapter 1.2). Both iron sources were directly used for iron oleate synthesis without further purification / drying.

Determination of the CO_2 content in the $FeCO_3$ and $Fe_2(CO_3)_3$. The composition of the $FeCO_3$ and $Fe_2(CO_3)_3$ was analyzed by reacting with sulfuric acid and measuring the released CO_2 content. For this experiment, $FeCO_3$ (1.70 g, 14.6 mmol) was prepared as described above. Sulfuric acid was added to the salt resulting in the release of the gas. After addition, the formulation starts to foam, while the generated CO_2 gas was captured in a measuring cylinder. The capped gas volume corresponds to the $FeCO_3$ was ~300 mL and differed 6% from the theoretically calculated value of 320 mL.

For the determination of the CO_2 content in the $Fe_2(CO_3)_3$, the same experiment was performed as described above. Sulfuric acid was added to $Fe_2(CO_3)_3$ (1.90 g, 6.51 mmol). The volume of the released gas was ~70 mL. This corresponds to a content of 16% $Fe_2(CO_3)_3$, while the rest of the salt is most probably $Fe(OH)_3$/ FeO(OH).

Synthesis of Fe(II) oleate. The synthesis of iron(II) oleate was carried out according to a self-developed procedure. The purified $FeCO_3$ salt (5.69 g, 51.4 mmol) was mixed with oleic acid (102.4 g, 362.4 mmol, 7-fold excess to Fe) at room temperature. The dispersion was heated to 60 °C, while stirring for 1 h, and cooled down to room temperature. After

additional stirring at room temperature for 24 h, a milky gray emulsion was obtained (Figure SI 3 left). Water and CO_2 (reaction equation is shown in SI chapter 2.1) were removed by heating to 60 °C under vacuum for 2 h. During this process, the color changed to brownish black (Figure SI 3 right). For effective removal of water residues, the solution was subsequently heated under vacuum up to 120 °C for 1 – 2 h. This synthesis protocol can easily be upscaled by a factor of 7 by using the same concentrations but lager volumes.

Synthesis of Fe(III) oleate. The synthesis of iron(III) oleate was carried out in the same way as the synthesis of iron(II) oleate.

The purified $Fe_2(CO_3)_3$ salt (11.6 g, 39.8 mmol) was mixed with oleic acid (158.5 g, 561.2 mmol, 7-fold excess to Fe) at room temperature. Byproducts are iron(III) hydroxide and iron(III) oxide-hydroxide and the reaction of the byproducts with oleic acid leads also to iron oleate and water, thus not interfering with further processes (reaction equations are shown in SI chapter 2.2). The dispersion was heated up to 60 °C while stirring for 1 h. The resulting emulsion was cooled down to room temperature and stirred for 24 h

whereat the color changed from red to the typical reddish brown (Figure SI 4). Water and CO_2 were removed by heating to 60 °C under vacuum for 2 h. During this process the color changed to brownish black (Figure SI 4 right). For effective removal of water residues, the solution was subsequently heated under vacuum up to 120 °C for 1 - 2 h. This synthesis protocol can easily be upscaled by a factor of 4 by using the same concentrations but lager volumes.

Nanocrystal synthesis. Iron oxide nanocrystals were synthesized by thermal decomposition of the iron(II) oleate or iron(III) oleate, respectively. Figure SI 5 shows an image of a typical apparatus for the synthesis: A three-necked round-bottom flask was equipped with a Vigreux column, and distillation column. Iron oleate was constantly heated (6 °C/min) and the temperature was kept for 3 - 5 h between 330 °C and 350 °C (depending on the oleic acid/1-octadecene ratio).

Methods.

MALDI-TOF MS measurements. All MALDI-TOF MS spectra were recorded on an ultrafleXtreme mass spectrometer (Bruker Daltonik GmbH, Bremen, Germany) with smartbeam-II™ laser. Data acquisition was performed in positive reflector mode with a

mass range of m/z = 350 - 4,500 and 2,000 – 20,000 using flex control software version 3.3.

9-Nitroanthracene (9-NA) was used as matrix (12 mg/mL in dry chloroform). All data evaluation and processing were performed using flexAnalysis version 3.3 (Bruker Daltonik GmbH, Bremen, Germany).

External calibration was performed with the peptide II standard in 2,5-dihydroxybenzoic acid (DHB, both Bruker Daltonik). After an initial evaluation of the data, spectra were also internally calibrated in cooperation with Dr. Volker Sauerland (Bruker Daltonik).

Peaks were selected for LIFT (MS/MS) measurements when showing an isotopic distribution indicating an iron complex.

The matrix and the sample (diluted wit dry toluene 1:25) were mixed with dry chloroform on a ground steel target in a glove box and then transferred to the MALDI-TOF MS using a Schlenk bag. Although every precaution has been taken, the contact with air (1 second max.) cannot be ruled out entirely.

Influence of the degree of purity of the used oleic acid on the MALDI-TOF spectra. For the synthesis of iron oleate pure oleic acid was used, because the use of technical grade

oleic acid causes additional peaks in the MALDI-TOF spectra. This is exemplified by the m/z = 955.6 ($[(Fe^{II})_2(OA^-)_3]^+$) peak using technical grade oleic acid (Figure SI 8 a) and pure oleic acid (Figure SI 8 b). The additional peaks at m/z = 951.6 and 952.6 and changes in intensities at 953.6 Da and 954.6 Da are due to linoleic acid, the typical contaminant in the technical grade of oleic acid.

Exemplarily, the calculations were refined by including a fraction of 10% of linoleic acid (LA), providing an even better fit for the experimental data of the reactions with technical grade oleic acid. This amount is in the range of the suppliers data on the purity of the oleic acid batch used. (Telephone-Information from the supplier Sigma-Aldrich).

Gas chromatography measurements. Gas chromatography measurements were carried out on a Perkin Elmer Clarus 500 instrument equipped with thermal conductivity detector (TCD). Helium was used as carrier gas with the constant flow rate of 85 ml/min. The column was packed with molecular sieve (5A 45/60 mesh (SUPELCO)). Temperatures: oven: 230 °C, TCD: 200 °C.

TEM measurements.

TEM and HRTEM. measurements were carried out on a JEOL JEM 1011 at 100 kV and on a JEOL JEM 2200 FS at 200 kV equipped with two CEOS Cs correctors (CETCOR, CESCOR) and a Gatan 4K UltraScan 1000 camera. To investigate the nanoparticles a drop of the diluted colloidal solution was deposited on a carbon coated 400 mesh TEM grid. The excess of solvent was removed with a filter paper and the grid was air dried.

High-Resolution HAADF-STEM imaging. High resolution HAADF-STEM images were acquired using an aberration-corrected cubed FEI-Titan electron microscope at an operating voltage of 300 kV. A camera length of 115 mm was used to guarantee incoherent imaging of the nanoparticles.

Electron tomography. The HAADF-STEM tilt series was acquired using a FEI Tecnai G2 electron microscope operated at 200 kV. For the acquisition of the tilt series a Fischione model 2020 singe tilt holder was used and the series was acquired using a tilt range from -74° to +74° with a tilt increment of 2°. The projection images were aligned using a cross-correlation algorithm together with a manual tilt axis adjustment implemented in the FEI Inspect3D software[50] and the reconstruction was performed using a total variation minimization reconstruction algorithm to minimize artefacts in the reconstruction.[51]

Electron energy loss spectroscopy (EELS) tomography. EELS experiments were performed using an aberration-corrected cubed FEI-Titan electron microscope operating at 120 kV. For the acquisition of the tilt series a Fischione model 2020 singe tilt holder was used and the series was acquired using a tilt range from -65° to +65° with a tilt increment of 10°. To reduce sample drift during the experiment, the specimen holder was allowed to relax after each tilting step for several minutes before image acquisition. EELS tomography series were reconstructed according to the procedure of Goris *et al.*[32]

SEM measurements. SEM investigations were carried out on a LEO 1550 SEM at 20 kV. The same nanoparticle-dispersion (SPIONs dispersed in toluene), as for the TEM measurements, was dropped on a silicon wafer and dried under air. The silicon wafer was then fixed on a standard SEM specimen holder.

XRD measurements. X-ray diffraction (XRD) patterns of the Iron oxide NC were recorded by using CuK_{α} (λ = 0.15418 nm) radiation (40 kV, 110 mA) on a X`Pert PRO MPD (*Philips*) diffractometer in the range of 30 to 110°/2θ.

The measurements were carried out in thin-walled (0.1 mm) XRD capillary tubes with 0.7 mm diameter and 80 mm length. To avoid oxidation, the capillary tubes were filled with purified NC dispersions and sealed in a glovebox.

Magnetic measurements. FeOx suspension had been transferred into Quantum Design VSM powder sample holders (P125E) and dried in inert gas atmosphere. Subsequently, the samples were measured in a Quantum Design Dynacool system equipped with the vibrating sample magnetometry (VSM) option between 5 and 350 K and in magnetic fields up to 30 kOe.

AUTHOR INFORMATION

Corresponding Authors

* weller@chemie.uni-hamburg.de, feld@chemie.uni-hamburg.de

Author Contributions

The manuscript was written through contributions of all authors. All authors have given approval to the final version of the manuscript. ‡These authors contributed equally.

ACKNOWLEDGMENT

The authors gratefully acknowledge financial support from the Deutsche Forschungsgemeinschaft (DFG, German Research Foundation) – Projektnummer 192346071 – SFB 986 and the excellence cluster 'The Hamburg Centre for Ultrafast Imaging - Structure, Dynamics and Control of Matter at the Atomic Scale' (by grant EXC 1074) S.B. and N.W. acknowledge financial support from European Research Council (ERC Starting Grant #335078-COLOURATOMS) and from the Research Foundation Flanders (FWO, Belgium) through Project fundings G038116N. Dr. Volker Sauerland for his support in calibrating the MALDI-TOF spectra. Almut Bark for measuring XRD.

Supporting Information Available: Chemistry of Shape-controlled Iron Oxide Nanocrystal Formation. This material is available free of charge *via* the Internet at http://pubs.acs.org.

REFERENCES

(1) Wu, L.; Mendoza-Garcia, A.; Li, Q.; Sun, S. Organic Phase Syntheses of Magnetic Nanoparticles and Their Applications. *Chem. Rev.* **2016**, *116*, 10473–10512.

(2) Smith, B. R.; Gambhir, S. S. Nanomaterials for *In Vivo* Imaging. *Chem. Rev.* **2017**, *117*, 901–986.

(3) Feld, A.; Merkl, J.-P.; Kloust, H.; Flessau, S.; Schmidtke, C.; Wolter, C.; Ostermann, J.; Kampferbeck, M.; Eggers, R.; Mews, A.; Schotten, T.; Weller, H. A Universal Approach to Ultrasmall Magneto-Fluorescent Nanohybrids. *Angew. Chemie Int. Ed.* **2015**, *54*, 12468–12471.

(4) Gleich, B.; Weizenecker, J. Tomographic Imaging Using the Nonlinear Response of Magnetic Particles. *Nature* **2005**, *435*, 1214–1217.

(5) Dreyer, A.; Feld, A.; Kornowski, A.; Yilmaz, E. D.; Noei, H.; Meyer, A.; Krekeler, T.; Jiao, C.; Stierle, A.; Abetz, V.; Weller, H. Organically Linked Iron Oxide Nanoparticle Supercrystals with Exceptional Isotropic Mechanical Properties. *Nat. Mater.* **2016**, *15*, 522–528.

(6) Demortière, A.; Panissod, P.; Pichon, B. P.; Pourroy, G.; Guillon, D.; Donnio, B.; Bégin-Colin, S. Size-Dependent Properties of Magnetic Iron Oxidenanocrystals. *Nanoscale* **2011**, *3*, 225–232.

(7) Wei, W.; Zhaohui, W.; Taekyung, Y.; Changzhong, J.; Woo-Sik, K. Recent Progress on Magnetic Iron Oxide Nanoparticles: Synthesis, Surface Functional Strategies and Biomedical Applications. *Sci. Technol. Adv. Mater.* **2015**, *16*, 23501.

(8) Zhao, Z.; Zhou, Z.; Bao, J.; Wang, Z.; Hu, J.; Chi, X.; Ni, K.; Wang, R.; Chen, X.; Chen, Z.; Gao, J. Octapod Iron Oxide Nanoparticles as High-Performance T_2 Contrast Agents for Magnetic Resonance Imaging. *Nat. Commun.* **2013**, *4*, 2266.

(9) Salazar-Alvarez, G.; Qin, J.; Šepelák, V.; Bergmann, I.; Vasilakaki, M.; Trohidou, K. N.; Ardisson, J. D.; Macedo, W. A. A.; Mikhaylova, M.; Muhammed, M.; Baró, M. D.; Nogués, J. Cubic *versus* Spherical Magnetic Nanoparticles: The Role of Surface Anisotropy. *J. Am. Chem. Soc.* **2008**, *130*, 13234–13239.

(10) Parkinson, G. S. Iron Oxide Surfaces. *Surf. Sci. Rep.* **2016**, *71*, 272–365.

(11) Sun, X.; Frey Huls, N.; Sigdel, A.; Sun, S. Tuning Exchange Bias in Core/Shell FeO/Fe 3 O 4 Nanoparticles. *Nano Lett.* **2012**, *12*, 246–251.

(12) Kavich, D. W.; Dickerson, J. H.; Mahajan, S. V.; Hasan, S. A.; Park, J.-H. Exchange

Bias of Singly Inverted FeO/Fe3O4 Core-Shell Nanocrystals. *Phys. Rev. B* **2008**, *78*, 174414.

(13) Park, J.; An, K.; Hwang, Y.; Park, J.-G.; Noh, H.-J.; Kim, J.-Y.; Park, J.-H.; Hwang, N.-M.; Hyeon, T. Ultra-Large-Scale Syntheses of Monodisperse Nanocrystals. *Nat. Mater.* **2004**, *3*, 891–895.

(14) Sun, S.; Zeng, H. Size-Controlled Synthesis of Magnetite Nanoparticles. *J. Am. Chem. Soc.* **2002**, *124*, 8204–8205.

(15) Yu, W. W.; Falkner, J. C.; Yavuz, C. T.; Colvin, V. L. Synthesis of Monodisperse Iron Oxide Nanocrystals by Thermal Decomposition of Iron Carboxylate Salts. *Chem. Commun.* **2004**, 2306.

(16) Hyeon, T.; Lee, S. S.; Park, J.; Chung, Y.; Na, H. B. Synthesis of Highly Crystalline and Monodisperse Maghemite Nanocrystallites without a Size-Selection Process. *J. Am. Chem. Soc.* **2001**, *123*, 12798–12801.

(17) Kwon, S. G.; Piao, Y.; Park, J.; Angappane, S.; Jo, Y.; Hwang, N.-M.; Park, J.-G.;

Hyeon, T. Kinetics of Monodisperse Iron Oxide Nanocrystal Formation by "Heating-Up" Process. *J. Am. Chem. Soc.* **2007**, *129*, 12571–12584.

(18) Kim, B. H.; Shin, K.; Kwon, S. G.; Jang, Y.; Lee, H.-S.; Lee, H.; Jun, S. W.; Lee, J.; Han, S. Y.; Yim, Y.-H.; Kim, D.-H.; Hyeon, T. Sizing by Weighing: Characterizing Sizes of Ultrasmall-Sized Iron Oxide Nanocrystals Using MALDI-TOF Mass Spectrometry. *J. Am. Chem. Soc.* **2013**, *135*, 2407–2410.

(19) Bronstein, L. M.; Huang, X.; Retrum, J.; Schmucker, A.; Pink, M.; Stein, B. D.; Dragnea, B. Influence of Iron Oleate Complex Structure on Iron Oxide Nanoparticle Formation. *Chem. Mater.* **2007**, *19*, 3624–3632.

(20) Kloust, H.; Zierold, R.; Merkl, J.-P.; Schmidtke, C.; Feld, A.; Pöselt, E.; Kornowski, A.; Nielsch, K.; Weller, H. Synthesis of Iron Oxide Nanorods Using a Template Mediated Approach. *Chem. Mater.* **2015**, *27*, 4914–4917.

(21) Bronstein, L. M.; Atkinson, J. E.; Malyutin, A. G.; Kidwai, F.; Stein, B. D.; Morgan, D. G.; Perry, J. M.; Karty, J. A. Nanoparticles by Decomposition of Long Chain Iron Carboxylates: From Spheres to Stars and Cubes. *Langmuir* **2011**, *27*, 3044–3050.

(22) Kemp, S. J.; Ferguson, R. M.; Khandhar, A. P.; Krishnan, K. M. Monodisperse Magnetite Nanoparticles with Nearly Ideal Saturation Magnetization. *RSC Adv.* **2016**, *6*, 77452–77464.

(23) Oh, S. M.; Henderickson, D. N.; Hassett, K. L.; Davis, R. E. Valence-Detrapping Modes for Electron Transfer in the Solid State of Mixed-Valence, Oxo-Centered, Trinuclear Iron Acetate Complexes: X-Ray Structure and Physical Data for [Fe3O(O2CCH3)6(4-Et-Py)3](4-Et-Py). *J. Am. Chem. Soc.* **1985**, *107*, 8009–8018.

(24) Lippard, S. J. Oxo-Bridged Polyiron Centers in Biology and Chemistry. *Angew. Chemie Int. Ed. English* **1988**, *27*, 344–361.

(25) Abrahamson, H. B.; Lukaski, H. C. Synthesis and Characterization of Iron Stearate Compounds. *J. Inorg. Biochem.* **1994**, *54*, 115–130.

(26) Chen, C. J.; Lai, H. Y.; Lin, C. C.; Wang, J. S.; Chiang, R. K. Preparation of Monodisperse Iron Oxide Nanoparticles *via* the Synthesis and Decomposition of Iron Fatty Acid Complexes. *Nanoscale Res. Lett.* **2009**, *4*, 1343–1350.

(27) Cannon, R. D.; White, R. P. Chemical and Physical Properties of Triangular Bridged Metal Complexes. In *Progress in Inorganic Chemistry*; John Wiley & Sons, Inc., 2007; pp 195–298.

(28) Ito, S.; Inoue, K.; Mastumoto, M. [Fe3O(OCOR)6L3]+-Catalyzed Epoxidation of Olefinic Alcohol Acetates by Molecular Oxygen. *J. Am. Chem. Soc.* 1982, *104*, 6450–6452.

(29) Barton, D. H. R.; Boivin, J.; Gastiger, M.; Morzycki, J.; Hay-Motherwell, R. S.; Motherwell, W. B.; Ozbalik, N.; Schwartzentruber, K. M. Functionalization of Saturated Hydrocarbons. Part 4. The Gif System for Selective Oxidation Using Molecular Oxygen. *J. Chem. Soc. Perkin Trans. 1* 1986, No. 4, 947.

(30) Murata, S.; Miura, M.; Nomura, M. Fe 3 O(OAc) 6 (Py) 3 Mediated Reduction of Aromatic Nitro Compounds with 2-Mercaptoethanol. *Chem. Lett.* 1988, *17*, 361–362.

(31) Chen, R.; Christiansen, M. G.; Sourakov, A.; Mohr, A.; Matsumoto, Y.; Okada, S.; Jasanoff, A.; Anikeeva, P. High-Performance Ferrite Nanoparticles through

Nonaqueous Redox Phase Tuning. *Nano Lett.* **2016**, *16*, 1345–1351.

(32) Goris, B.; Meledina, M.; Turner, S.; Zhong, Z.; Batenburg, K. J.; Bals, S. Three Dimensional Mapping of Fe Dopants in Ceria Nanocrystals Using Direct Spectroscopic Electron Tomography. *Ultramicroscopy* **2016**, *171*, 55–62.

(33) Goris, B.; Turner, S.; Bals, S.; Van Tendeloo, G. Three-Dimensional Valency Mapping in Ceria Nanocrystals. *ACS Nano* **2014**, *8*, 10878–10884.

(34) Jarausch, K.; Thomas, P.; Leonard, D. N.; Twesten, R.; Booth, C. R. Four-Dimensional STEM-EELS: Enabling Nano-Scale Chemical Tomography. *Ultramicroscopy* **2009**, *109*, 326–337.

(35) Möbus, G.; Doole, R. C.; Inkson, B. J. Spectroscopic Electron Tomography. *Ultramicroscopy* **2003**, *96*, 433–451.

(36) Möbus, G.; Inkson, B. J. Three-Dimensional Reconstruction of Buried Nanoparticles by Element-Sensitive Tomography Based on Inelastically Scattered Electrons. *Appl. Phys. Lett.* **2001**, *79*, 1369–1371.

(37) Nicoletti, O.; de la Peña, F.; Leary, R. K.; Holland, D. J.; Ducati, C.; Midgley, P. A. Three-Dimensional Imaging of Localized Surface Plasmon Resonances of Metal Nanoparticles. *Nature* **2013**, *502*, 80–84.

(38) Yedra, L.; Eljarrat, A.; Arenal, R.; Pellicer, E.; Cabo, M.; López-Ortega, A.; Estrader, M.; Sort, J.; Baró, M. D.; Estradé, S.; Peiró, F. EEL Spectroscopic Tomography: Towards a New Dimension in Nanomaterials Analysis. *Ultramicroscopy* **2012**, *122*, 12–18.

(39) Pichon, B. P.; Gerber, O.; Lefevre, C.; Florea, I.; Fleutot, S.; Baaziz, W.; Pauly, M.; Ohlmann, M.; Ulhaq, C.; Ersen, O.; Pierron-Bohnes, V.; Panissod, P.; Drillon, M.; Begin-Colin, S. Microstructural and Magnetic Investigations of Wüstite-Spinel Core-Shell Cubic-Shaped Nanoparticles. *Chem. Mater.* **2011**, *23*, 2886–2900.

(40) Chen, C.-J.; Chiang, R.-K.; Lai, H.-Y.; Lin, C.-R. Characterization of Monodisperse Wüstite Nanoparticles Following Partial Oxidation. *J. Phys. Chem. C* **2010**, *114*, 4258–4263.

(41) Wetterskog, E.; Tai, C.; Grins, J.; Bergström, L.; Salazar-Alvarez, G. Anomalous

Magnetic Properties of Nanoparticles Arising from Defect Structures: Topotaxial Oxidation of Fe 1– x O|Fe 3−δ O 4 Core|Shell Nanocubes to Single-Phase Particles. *ACS Nano* **2013**, *7*, 7132–7144.

(42) Stamps, R. L. Mechanisms for Exchange Bias. *J. Phys. D. Appl. Phys.* **2000**, *33*, R247–R268.

(43) Schrettle, F.; Kant, C.; Lunkenheimer, P.; Mayr, F.; Deisenhofer, J.; Loidl, A. Wüstite: Electric, Thermodynamic and Optical Properties of FeO. *Eur. Phys. J. B* **2012**, *85*, 164.

(44) Walz, F. The Verwey Transition - a Topical Review. *J. Phys. Condens. Matter* **2002**, *14*, R285–R340.

(45) Khurshid, H.; Li, W.; Chandra, S.; Phan, M.-H.; Hadjipanayis, G. C.; Mukherjee, P.; Srikanth, H. Mechanism and Controlled Growth of Shape and Size Variant Core/Shell FeO/Fe3O4 Nanoparticles. *Nanoscale* **2013**, *5*, 7942–7952.

(46) Bau, J. A.; Li, P.; Marenco, A. J.; Trudel, S.; Olsen, B. C.; Luber, E. J.; Buriak, J. M.

Nickel/Iron Oxide Nanocrystals with a Nonequilibrium Phase: Controlling Size, Shape, and Composition. *Chem. Mater.* **2014**, *26*, 4796–4804.

(47) Xia, Y.; Xia, X.; Peng, H.-C. Shape-Controlled Synthesis of Colloidal Metal Nanocrystals: Thermodynamic *versus* Kinetic Products. *J. Am. Chem. Soc.* **2015**, *137*, 7947–7966.

(48) Shin, D.; Kim, M.; Song, H. Selective Growth and Structural Analysis of Regular MnO Nanooctapods Bearing Multiple High-Index Surface Facets. *Chem. - An Asian J.* **2015**, *10*, 1784–1790.

(49) Cho, K.-S.; Talapin, D. V.; Gaschler, W.; Murray, C. B. Designing PbSe Nanowires and Nanorings through Oriented Attachment of Nanoparticles. *J. Am. Chem. Soc.* **2005**, *127*, 7140–7147.

(50) Schoenmakers, R. H. M.; Perquin, R. A.; Fliervoet, T. F.; Voorhout, W. High Resolution, High Throughput Electron Tomography Reconstruction. *Microsc. Microanal.* **2005**, *11*, 312–313.

(51) Goris, B.; Van den Broek, W.; Batenburg, K. J.; Heidari Mezerji, H.; Bals, S. Electron Tomography Based on a Total Variation Minimization Reconstruction Technique. *Ultramicroscopy* **2012**, *113*, 120–130.